PHILOSOPHICAL TRANSACTIONS A

rsta.royalsocietypublishing.org

Research

Cite this article: Wiesman HS, Zimmerman ME, Kohlstedt DL. 2018 Laboratory investigation of mechanisms for phase mixing in olivine + ferropericlase aggregates. *Phil. Trans. R. Soc. A* **376**: 20170417.
http://dx.doi.org/10.1098/rsta.2017.0417

Accepted: 24 July 2018

One contribution of 14 to a discussion meeting issue 'Earth dynamics and the development of plate tectonics'.

Subject Areas:
plate tectonics, geophysics

Keywords:
phase mixing, Zener pinning, mechanical weakening, torsional deformation, olivine, ferropericlase or magneseowüstite

Author for correspondence:
Harison S. Wiesman
e-mail: wiesm010@umn.edu

Laboratory investigation of mechanisms for phase mixing in olivine + ferropericlase aggregates

Harison S. Wiesman[1], Mark E. Zimmerman[2] and David L. Kohlstedt[2]

[1]School of Physics and Astronomy, and [2]Department of Earth Sciences, University of Minnesota Twin Cities, Minneapolis, MN 55455, USA

DLK, 0000-0002-6417-6465

To investigate the role of grain boundary pinning and the mechanisms by which phase mixing occurs during deformation of polymineralic rocks, we conducted high-strain torsion experiments on samples consisting of olivine plus 30 vol% ferropericlase. Experiments were performed in a gas-medium deformation apparatus at 1524 K and 300 MPa. Samples were deformed to outer radius shear strains of up to $\gamma(R) = 14.1$. The value of the stress exponent and the small grain sizes of our samples indicate that our two-phase material deformed by dislocation-accommodated grain boundary sliding. In samples deformed to $1 < \gamma < 7$, elongated clusters of ferropericlase grains form thin layers in the olivine matrix, and small grains of ferropericlase appear at olivine grain boundaries and three- and four-grain junctions. By $\gamma \approx 14$, a well-distributed mixture of small ferropericlase grains among the olivine grains developed. Microstructures exhibit similarities to both mechanical and chemical models proposed to describe the processes leading to phase mixing. Our results provide evidence for grain size reduction during phase mixing that results in a grain size significantly smaller than the value predicted by the single-phase recrystallization piezometer for olivine. Thus, phase mixing provides a mechanism for the persistent weakening of rocks that is important for developing and maintaining shear zones necessary for plate tectonics.

THE ROYAL SOCIETY PUBLISHING

This article is part of a discussion meeting issue 'Earth dynamics and the development of plate tectonics'.

1. Introduction

On Earth, large-scale ductile shear zones allow for the motion of tectonic plates past one another at plate boundaries. The formation and continued operation of such features require mechanisms for strain weakening and long-term localization of strain into relatively narrow bands [1,2]. Localization can occur due to a combination of weakening processes associated with water, melt, shear heating, pre-existing crystallographic preferred orientation (CPO), or grain size reduction in regions of deformation [3–5]. In natural samples of peridotite from exhumed shear zones, the strain is often localized in fine-grained mylonites and ultramylonites in which grains of secondary phases are thoroughly mixed with the primary olivine grains [5–8]. Particles of a secondary phase act at the grain scale to pin olivine grain boundaries, thus retarding grain growth. Inhibiting grain growth due to the prevalence of interphase boundaries allows deformation-driven reduction of grain size to values below that predicted by single-phase piezometers [9]. If the deformation of the rock is dominated by a grain size-sensitive mechanism, such as diffusion creep or dislocation-accommodated grain boundary sliding (disGBS), continued grain size reduction results in strain weakening that facilitates the localization of strain into thoroughly mixed, fine-grained regions.

While the theory of Zener pinning at interphase boundaries is well understood once grains of the major and minor phases have been thoroughly mixed [9–12], the physical mechanisms that control phase mixing and its onset at the grain scale during deformation are not well understood. Previous studies based on natural samples hypothesized that phase mixing could occur due to chemical and metamorphic reactions [13,14], fluid-assisted mechanisms [15] or brittle processes. Recent experimental studies on samples of calcite plus anhydrite and samples of olivine (Ol) plus orthopyroxene (Opx) investigated the underlying physical mechanisms that lead to mixing and subsequent strain weakening. Observations of the microstructures produced in these experiments led to a variety of explanations for the observed phase mixing. Cross & Skemer [16] proposed a mechanical mixing mechanism based on their experimental observations of sheared samples of calcite plus anhydrite in which large clusters of each phase are thinned and elongated with increasing strain until they form layers of a single grain thickness. These layers are then pulled apart at high strains leading to a well-mixed system whereby phase mixing is controlled by the strain required to thin out each layer. Bercovici & Skemer [17] suggested another mechanical mechanism for phase mixing in samples of Ol plus Opx in which small grains or 'teeth' of Ol form at Opx-Ol-Opx triple junctions. In response to the imposed stress gradient, these Ol 'teeth' migrate away from the Ol layer along Opx-Opx grain boundaries towards Opx triple junctions, thus causing mixing of the two phases. Tasaka *et al*. [18] explained phase mixing in their Ol plus Opx samples with a chemical mechanism based on (i) the fact that Ol and Opx share common chemical building blocks, MeO and SiO_2 and (ii) the appearance of small grains of Ol and Opx along grain boundaries of the opposite phase. They interpreted this feature as being due to stress gradients established during deformation driving diffusion of the faster component, MeO, from Ol grain boundaries in deviatoric compression to Opx grain boundaries in deviatoric tension. Owing to the slow diffusion speed of the SiO_2 component in this system [19–21], small grains of Opx are left behind at Ol grain boundaries, and the MeO reacts with the neighbouring Opx to form new, small grains of Ol at Opx grain boundaries. With continued deformation, this process would lead to a well-mixed microstructure.

To further investigate the possible role of chemical processes in phase mixing, we deformed two-phase aggregates composed of olivine plus ferropericlase (Fp) to high strain in torsion in a high-resolution, gas-medium apparatus. In contrast to the Ol plus Opx system in which the two phases are made up of the same building blocks, the two phases in the Ol plus Fp system share only the faster component, MeO. Therefore, if mixing is controlled by the relatively

rapid diffusion of MeO, then MeO units should diffuse from Fp grain boundaries in deviatoric compression to both Fp and Ol grain boundaries in deviatoric tension. As a result, small Fp grains are anticipated to appear along Ol grain boundaries in deviatoric tension, but no corresponding phase is expected along Fp grain boundaries. If instead a mechanical mechanism is responsible for the mixing, we might expect to see the formation of 'teeth' at Ol-Fp-Ol and Fp-Ol-Fp triple junctions accompanied by small particles of either phase along grain boundaries in deviatoric tension and at triple junctions nearby their parent layers. Such particles could also appear along grain boundaries in deviatoric compression if clusters of grains are thinned and pulled apart with increasing strain. In addition, the inclusion of Fp as a minor phase allowed us to examine the effects of a weaker secondary phase [22] on the rheological properties of two-phase samples.

2. Methods

(a) Sample preparation

Polycrystalline, two-phase samples were fabricated from a mixture of powders composed of 70% Ol plus 30% Fp; phase percentages (%) indicate vol% of each phase. To synthesize ferropericlase with the composition $(Mg_{0.9}Fe_{0.1})O$, 1–5 µm powders of MgO and Fe_2O_3 were dried overnight in a vacuum oven at a temperature, T, of 510 K and a pressure, P, of 10 kPa. These powders were then thoroughly mixed with an agate mortar and pestle in the appropriate molar proportions. The mixed powders were alloyed in an alumina crucible lined with Ni foil in a one-atmosphere horizontal furnace for 12 h at 1673 K at an oxygen partial pressure of 10^{-9} Pa set by a $CO:CO_2$ molar gas ratio of 1 : 22.3. The resulting powders were ground and mixed again with an agate mortar and pestle before annealing for an additional 12 h. This procedure was repeated five times to ensure the powders were compositionally homogeneous. Analyses of X-ray powder diffraction patterns verified that the resultant powder was ferropericlase.

The ferropericlase powder was subsequently mixed with San Carlos olivine (SC-Ol) powder with a particle size of 5.5 ± 2.2 µm to make a well-distributed mixture. This mixture was uniaxially cold-pressed into a cylindrical Ni capsule (inner diameter 12 mm, height 30 mm) with a central Ni post (diameter 8 mm) at room temperature and $P = 100$ MPa. An evacuated, isostatic hot-press was then performed on the cold-pressed sample in a gas-medium apparatus [23] at $T = 1523$ K with a confining pressure of 300 MPa and a vacuum pressure of 15 Pa for 2 h to produce a dense, two-phase aggregate. A single-phase, polycrystalline sample of SC-Ol was fabricated from the same starting SC-Ol powders as the two-phase sample. As with the two-phase sample, powders were cold-pressed into an Ni capsule with a central Ni post, followed by an evacuated, isostatic hot-press under the same temperature and confining pressure conditions as above and at a vacuum pressure of 20 Pa for 1 h to produce a dense, single-phase, thin-walled cylinder. The resulting thin-walled cylinders were cut into 2.5–3.0 mm thick discs for torsion experiments, as sketched in figure 1. Thin-walled samples created via this procedure minimize radial variations in stress and microstructure across the sample during torsional deformation [24,25].

(b) Deformation experiments

Assemblies for deformation experiments were prepared by placing a single disc of the hot-pressed sample between porous alumina spacers. Solid alumina and zirconia pistons were used to fill the rest of the assembly. The pistons were inserted into a thin-walled Fe jacket and loaded into a gas-medium deformation apparatus with a torsion actuator [25].

Samples were deformed in torsion at $T = 1523$ K and $P = 300$ MPa at a constant twist rate until the torque approached a steady-state value. Shear stress, τ, was calculated from the torque using the relevant relationship for a thin-walled cylinder [25], after subtracting the torque supported by the Ni capsule, Ni post and the Fe jacket [24,26]. Equivalent stress, σ, and equivalent strain rate, $\dot{\varepsilon}$, were calculated from τ and the shear strain rate, $\dot{\gamma}$, using the appropriate conversions [25].

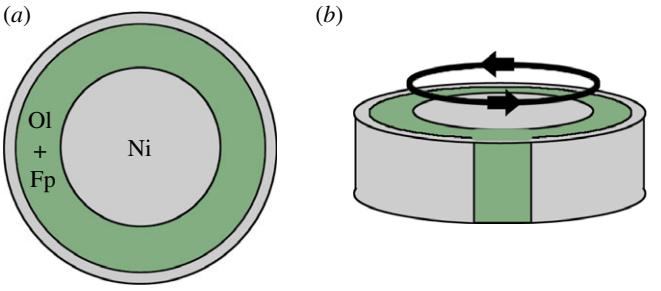

Figure 1. Schematic of a torsion sample. (*a*) Top-down drawing of a thin-walled cylindrical sample with the hot-pressed SC-Ol plus Fp sample encased in a Ni can with a central Ni post. (*b*) Drawing of a sample right-cylindrical disc for a torsion experiment with the direction of shear indicated. A tangential window into the sample is exposed and polished after the deformation experiment in order to view the microstructure of the sample.

Strain-rate steps were taken during the experiments once the torque approached a constant value in order to determine the value of the stress exponent, n, in a power-law flow law of the form

$$\dot{\varepsilon} = A\frac{\sigma^n}{d^p}, \tag{2.1}$$

where A is a material-dependent parameter, d is the grain size and p is the grain size exponent. At each new value of $\dot{\gamma}$, a new, roughly constant value of torque was reached after the accumulation of shear strain, γ, of $\Delta\gamma \approx 0.1$. The amount of strain accumulated at the new rate was kept as low as possible and the twist rate returned to the original value between steps to minimize the change in microstructure associated with the new shear stress, such that n was determined at a constant grain size [24].

(c) Microstructural analysis

The microstructures of the deformed and undeformed samples were analysed by exposing a tangential section of each cylindrical sample. This step was accomplished by removing the metal jacket around the sample on an SiC grinding wheel, then polishing a tangent to the cylinder using diamond lapping film down to a 0.5 µm grit size, followed by a chemical–mechanical polish with 40 nm colloidal silica. Samples were then etched to reveal grain and phase boundaries, either with a diluted mixture of HF + HCl or by heating at 1423 K for 0.5 h at an oxygen partial pressure of 4×10^{-9} Pa in a $CO:CO_2$ molar gas ratio of 1 : 5.9.

High-resolution images were acquired with a Hitachi S-4700 field-emission gun, scanning electron microscope (SEM) at an accelerating voltage of 15 kV and a beam current of 10 µA. A 4–5 Å carbon coat was deposited on the samples to prevent charging during SEM analysis. After tracing individual grains of both phases, grain sizes of the two phases were determined by calculating the equivalent diameters from their equivalent areas with the ImageJ software, then fitting the grain size distributions to a lognormal distribution. Grain boundary and phase boundary fractions were measured similarly by calculating the length of Ol-Ol, Fp-Fp and Ol-Fp interfaces with ImageJ.

3. Results

(a) Microstructural results

Backscattered electron (BSE) micrographs from tangential sections of the undeformed sample and four samples deformed in torsion are displayed in figure 2. Grain size distributions determined from similar images for each sample are given in figure 3. The Fp is well distributed throughout

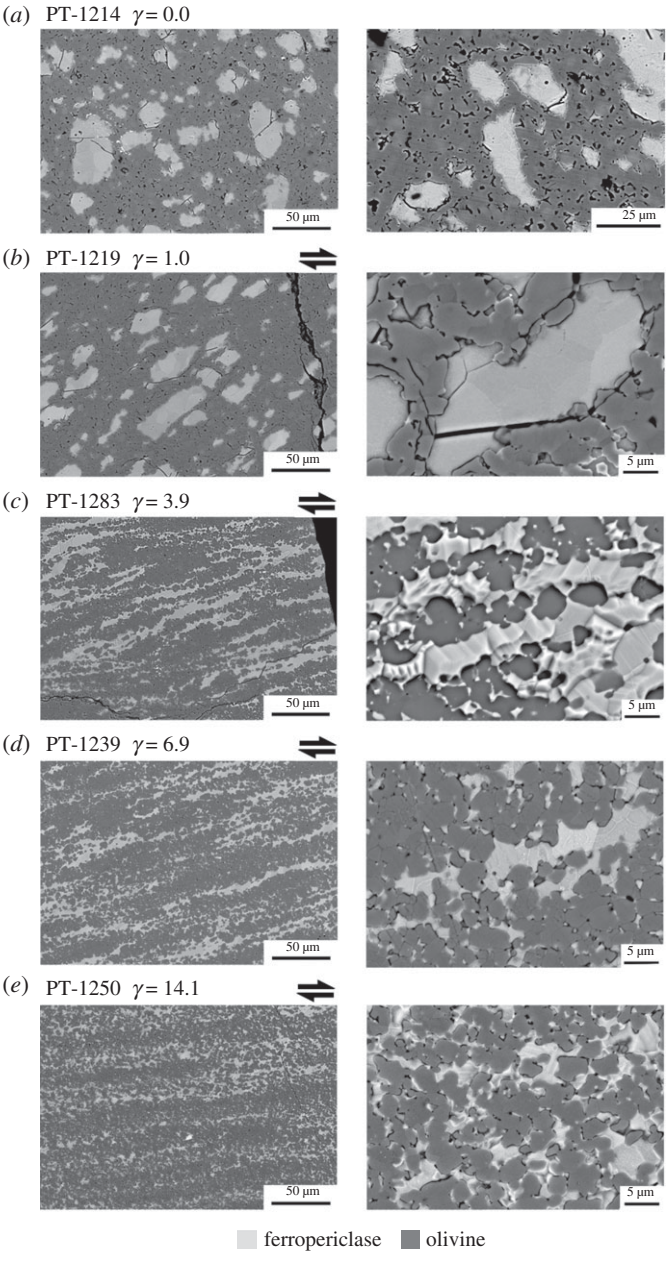

Figure 2. BSE images of the microstructures of undeformed and deformed samples at two different scales for the following samples: (*a*) Undeformed, hot-pressed sample (PT-1214), (*b*) sample deformed to $\gamma = 1.0$ (PT-1219), (*c*) sample deformed to $\gamma = 3.9$ (PT-1283), (*d*) sample deformed to $\gamma = 6.9$ (PT-1239) and (*e*) sample deformed to $\gamma = 14.1$ (PT-1250). For the deformed samples, the direction of shear is top to the right.

the matrix of Ol in the starting material (figure 2*a*). The Ol grain size in the hot-pressed material is $d_{Ol} = 3.7 \pm 0.2\,\mu m$. Clustered regions of Fp grains, which vary significantly in size from 10 to 60 µm, generally consist of multiple grains with an average grain size of $d_{Fp} = 3.6 \pm 0.4\,\mu m$.

At low shear strains $\gamma \approx 1.0$, domains of Fp are elongated in the direction of shear at an angle of $42° \pm 2°$ to the shear plane (figure 2*b*). The average grain sizes of the two phases have decreased to $d_{Ol} = 3.0 \pm 0.2\,\mu m$ and $d_{Fp} = 2.4 \pm 0.2\,\mu m$.

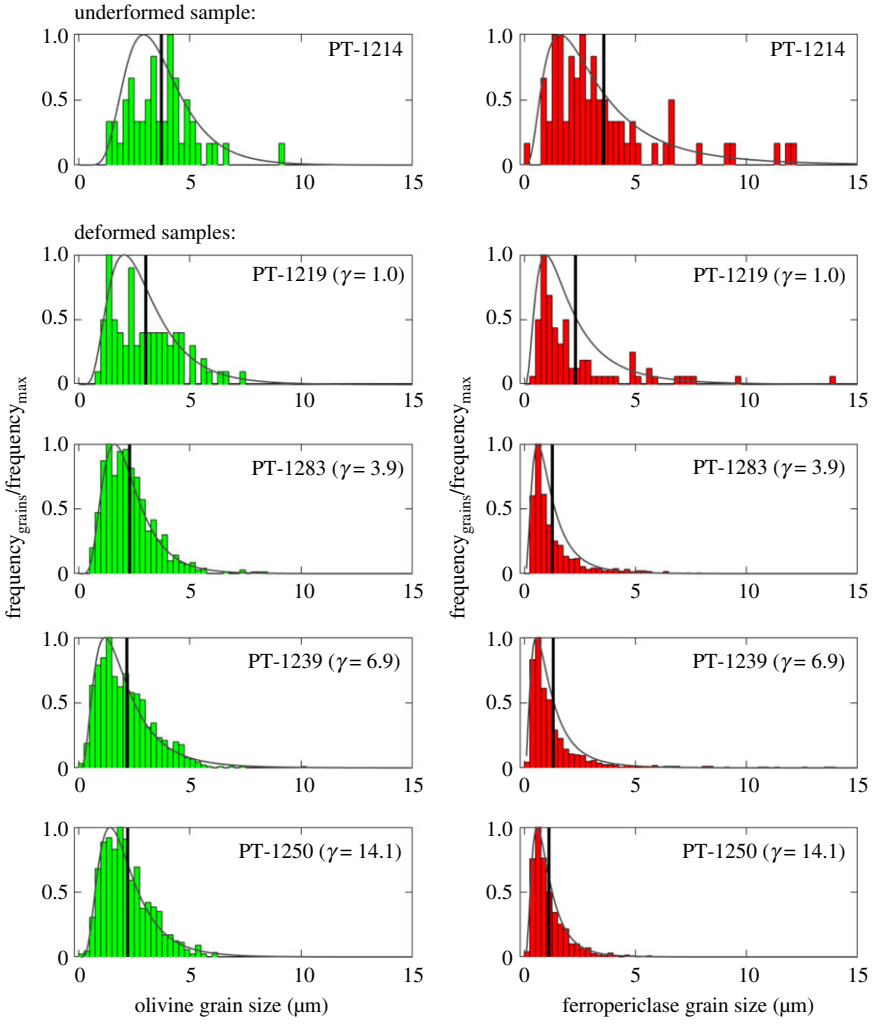

Figure 3. Grain size distribution normalized to the maximum frequency of grains for each experiment. Grain size was calculated via the equivalent area method. The black curve represents the lognormal distribution fit to each grain size distribution. The vertical black line represents the mean grain size of each distribution calculated from the lognormal fit.

In samples deformed to shear strains in the range $3.0 \leq \gamma \leq 7.0$, clusters of Fp grains have been further thinned and elongated; with increasing strain, these layers lie at an angle of $20° \pm 2°$ to $15° \pm 2°$ to the shear plane (figure 2*c*,*d*). At this point, Ol grains have impinged upon grains in the clusters of Fp, distorting the Fp. Small grains of Fp have started to appear along Ol grain boundaries and at Ol three- and four-grain junctions, driving the average grain size of Fp down to $d_{Fp} = 1.3 \pm 0.1$ µm, while a number of larger grains still exist in the centre of the Fp domains. The average Ol grain size in the matrix has decreased to $d_{Ol} = 2.2 \pm 0.1$ µm, and individual grains appear between domains of Fp.

At $\gamma \geq 14$, layers of Fp can still be identified, now at an angle of $4° \pm 1°$ to the shear plane. Individual domains of Fp are no longer distinguishable; that is, no large grains or clusters of Fp remain (figure 2*e*). Small Fp grains are thoroughly distributed throughout the Ol matrix, and the distribution in grain size has shifted to a smaller value overall. The average grain size of the Ol is $d_{Ol} = 2.2 \pm 0.1$ µm and the grain size of Fp has further decreased slightly to $d_{Fp} = 1.1 \pm 0.1$ µm.

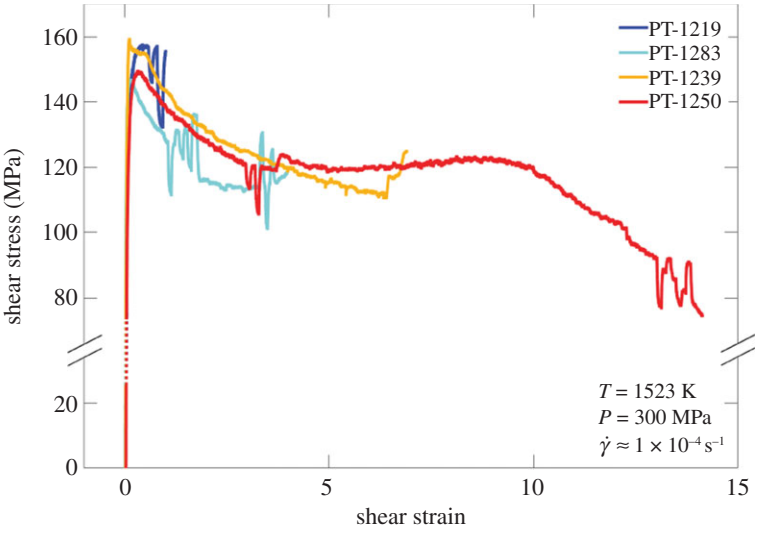

Figure 4. Shear stress versus shear strain data obtained from torsional deformation experiments performed on four samples of SC-Ol plus 30% Fp. Experiments were performed at $T = 1523$ K, $P = 300$ MPa, and an outer radius shear strain rate of $\dot{\gamma}(R) \approx 1.0 \times 10^{-4}\,s^{-1}$. Strain-rate excursions appear as steps in the curves.

(b) Mechanical data

In this study, each experiment was performed at the same initial shear strain rate determined at the outer radius, $\dot{\gamma}(R)$, of approximately $1 \times 10^{-4}\,s^{-1}$. All samples displayed similar mechanical behaviour, as seen in the plots of shear stress versus shear strain in figure 4. A peak shear stress of approximately 150 MPa was reached after a sample accumulated a shear strain of $\gamma = 0.2$–0.3, followed by a relatively rapid decrease of 30–40 MPa in shear stress by a shear strain of 3–4. The flow stress then remained roughly constant with increasing shear strain, aside from long periodicity sinusoidal noise introduced into the load measurement from off-axis loading of the sample during the duration of the experiment. For the sample deformed to $\gamma \approx 14$, the shear stress began to decrease again at $\gamma \approx 10$.

Based on analysis of the results from strain-rate steps in terms of equation (2.1), n was determined using a linear least-squares fit to the log–log plot of $\dot{\varepsilon}$ versus σ data in figure 5 for three of the experiments. Strain-rate steps taken in two experiments near the peak stress for $1 \leq \gamma \leq 2$ resulted in values of $n = 2.6 \pm 0.2$ and 4.8 ± 0.7. Steps taken in two experiments in the steady-state regime for $3 \leq \gamma \leq 4$ yielded $n = 3.6 \pm 0.5$ and 2.9 ± 0.2. Strain-rate steps taken during the high-strain experiment at $\gamma > 10$ yielded $n = 3.4 \pm 0.6$. For comparison, a shear stress versus shear strain curve from a torsion experiment carried out on an aggregate of single-phase SC-Ol is included in figure 6. A summary of mechanical and microstructural parameters is given in table 1.

4. Discussion

(a) Deformation mechanism

Triaxial compressive creep experiments performed in a gas-medium apparatus on single-phase aggregates of SC-Ol by Hansen *et al*. [27] and Wang *et al*. [28] resulted in flow laws for deformation in the disGBS regime with stress exponents of $n = 2.9 \pm 0.3$ and $n = 3.4 \pm 0.2$, respectively. Models of GBS predict a value of $n = 3$ or $n = 2$ for GBS with or without subgrain boundaries, respectively [29]. Additionally, torsion experiments performed in a gas-medium apparatus on fine-grained (15–32 µm) aggregates of SC-Ol yielded a stress exponent of $n = 3.2$–3.3 [30], while

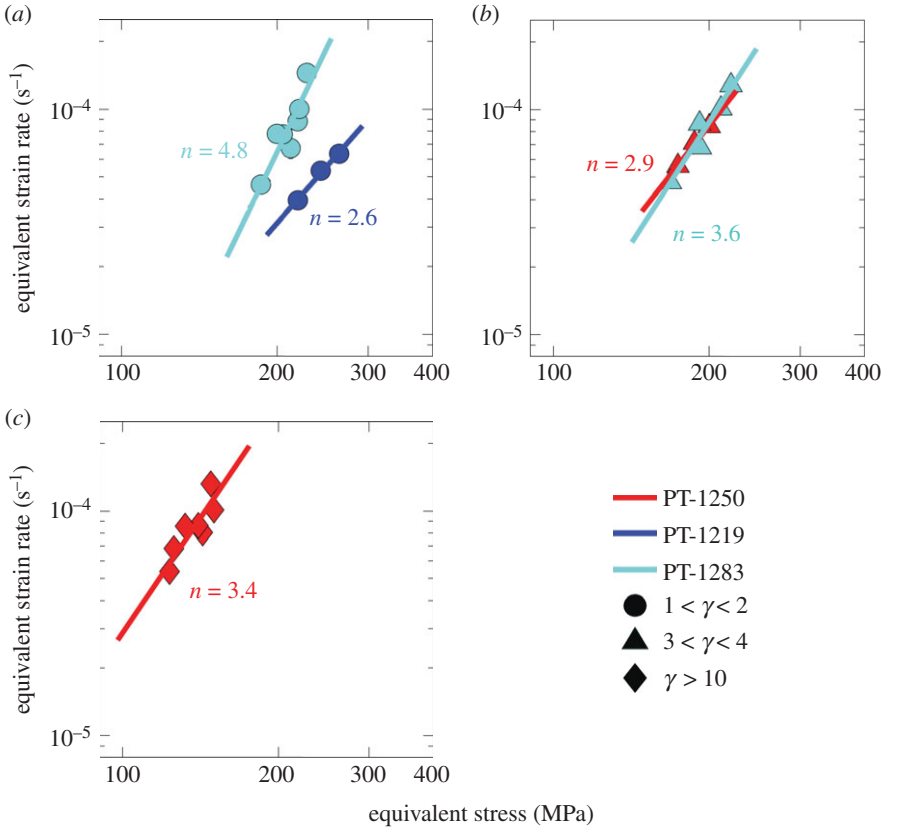

Figure 5. Equivalent strain rate versus equivalent stress plotted on a log–log scale for strain-rate steps taken at (*a*) $\gamma \approx 1.0$, (*b*) $\gamma \approx 3.0$ and (*c*) $\gamma \approx 13.0$. Solid lines are fits to the data from the strain-rate steps in each experiment used to calculate the stress exponent, *n*. Different symbols represent strain-rate steps taken at different shear strains. No strain-rate steps were taken during the experiment PT-1239.

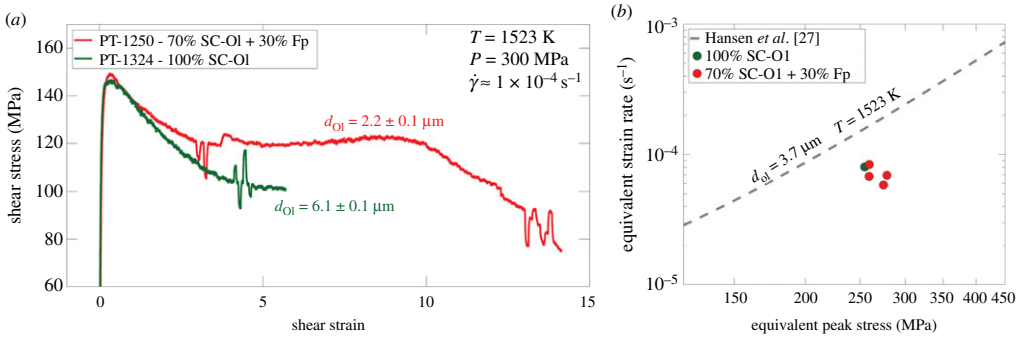

Figure 6. (*a*) Comparison of shear stress versus shear strain data for torsion experiments performed on single-phase SC-Ol and two-phase samples containing 70% SC-Ol + 30% Fp. Experiments were performed under the same conditions at $T = 1523$ K, $P = 300$ MPa, and an outer radius shear strain rate of $\dot{\gamma}(R) \approx 1.0 \times 10^{-4}$ s^{-1}. Ol grain sizes for each sample are listed by their respective samples. (*b*) Comparison of the peak shear stress in the single-phase SC-Ol sample and two-phase samples. For comparison, the flow law for disGBS in SC-Ol determined by Hansen *et al.* [27] in triaxial compressive creep experiments is plotted here at $T = 1523$ K and $d_{Ol} = 3.7$ µm, the Ol grain size in each sample at the peak stress.

Table 1. Summary of rheological and microstructural parameters for each experiment. The fraction of ferropericlase in each experiment was $f_{Fp} = 0.3$.[a]

	undeformed	deformed				
experiment ID:	PT-1214	PT-1219	PT-1283	PT-1239	PT-1250	PT-1324[b]
equivalent peak stress (MPa)	—	274.65	259.11	278.60	259.27	254.55
equivalent flow stress (MPa)	—	—	200.92	196.41	208.54	180.13
d_{Ol} (μm) [b]	3.7 ± 0.2	3.0 ± 0.2	2.3 ± 0.1	2.2 ± 0.1	2.2 ± 0.1	6.2 ± 0.1
d_{Fp} (μm) [b]	3.6 ± 0.4	2.4 ± 0.2	1.3 ± 0.1	1.3 ± 0.1	1.1 ± 0.1	n.a.
n	—	2.6 ± 0.2	2.9 ± 0.2, 3.4 ± 0.6	—	4.8 ± 0.7, 3.6 ± 0.5	3.8 ± 0.3
shear strain	0.0	1.0	3.9	6.9	14.1	5.7
equivalent strain rate (10^{-5} s^{-1})	—	5.83	6.75	6.87	8.37	8.04

[a]Experiment PT-1324 was performed on a sample consisting of single-phase polycrystalline San Carlos olivine, or $f_{Fp} = 0$.
[b]Reported grain sizes are the mean grain size determined from the fit of the grain size distribution to a lognormal distribution. Reported uncertainties are calculated from the standard deviation (s) from the distribution normalized by the number of grains analysed (N) as $s/\sqrt{N}$.

triaxial compression experiments on relatively coarse-grained (approx. 900 μm) samples of Åheim dunite resulted in a value of $n = 3.8 \pm 0.4$ [31]. The former likely deformed by disGBS, while the latter presumably deformed by dislocation creep. As another means of comparison, the stress exponent determined for the sample of single-phase SC-Ol deformed in this study (table 1; PT-1324) had a value of $n = 3.8 \pm 0.3$. The fine initial grain size of 3.7 ± 0.1 μm and final grain size of 6.2 ± 0.1 μm, along with the stress exponent implies this sample also likely deformed by disGBS.

The experiments on two-phase aggregates of SC-Ol plus Fp performed in this study yielded a stress exponent of $n = 2.6$–4.8. However, strain-rate steps taken in two experiments during the initial weakening stage of the material for $0.2 < \gamma < 2.0$ and in one experiment during the later weakening event for $\gamma \geq 10$ are not representative of steady-state flow. The nonlinear, downward-sloping behaviour of the shear stress versus shear strain curves during weakening in figure 4 demonstrates that flow stress does not return to its original value between rate steps, but instead returns to a lower value. This behaviour results in some rate steps performed at higher strain rates reaching stresses matching those measured just before at lower strain rates. Such mechanical weakening is likely due to the evolving microstructure at these values of shear strain; for example, the rapid decrease in flow stress with increasing strain following the peak stress has been associated primarily with a decrease in grain size and CPO development [24]. Considering only values of equivalent stress and equivalent strain rate determined from rate steps taken for two samples during steady-state flow for $3 < \gamma < 10$, a fit through all of the data results in an average stress exponent of $n = 3.4 \pm 0.4$ for the two-phase samples in this study. This value for n is within the error of the value for n determined in the sample of single-phase SC-Ol deformed in this study, which deformed by disGBS. Given the value of the stress exponent determined at constant microstructure in the steady-state portion of the shear stress versus shear strain curve (figure 5*b*) and the relatively small grain size of our samples, deformation likely occurred in the disGBS regime, a conclusion supported by the initial weakening observed at $\gamma \leq 3$.

A change in deformation mechanism due to grain size reduction induced by grain boundary pinning and signalled by a change in n was not observed at higher strains ($\gamma > 10$). However, as previously noted, experiment PT-1250 underwent mechanical weakening at $\gamma > 10$ (figure 4). As illustrated in figure 7*b*, this sample developed a region of strain localization near the centre of the sample. Unlike samples deformed to lower shear strains, PT-1250 was displaced in the radial direction along a narrow shear zone, without vertical shortening. Although strain-rate steps

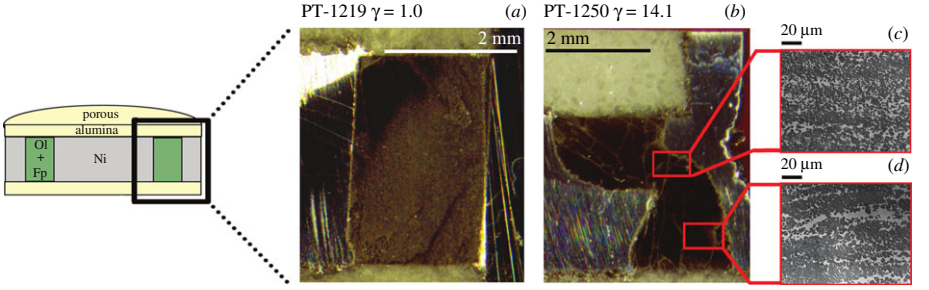

Figure 7. Optical photographs of radial sections of two different thin-walled cylindrical samples, one deformed to (*a*) low strain and the other to (*b*) high strain. Grey/silver areas are Ni, brown regions are SC-Ol plus Fp and off-white regions are porous alumina. Note the straight vertical edges of the sample deformed to $\gamma(R) = 1.0$ in contrast to the distorted edges of the sample to deformed $\gamma(R) = 14.1$ due to strain localization at high strain during deformation. The starting heights of the two samples were different; no shortening was observed during torsion experiments. Reflected light micrographs of the regions (*c*) inside and (*d*) outside of the shear zone that developed in the high-strain sample are also displayed here. The dark grey phase in these images is olivine, while the light grey phase is ferropericlase.

taken during such mechanical weakening do not yield a highly reliable value for n, the value of $n > 3$ nonetheless indicates that dislocation processes are an important part of the deformation mechanism, consistent with deformation in the disGBS regime.

(b) Comparison with previous results

The peak stresses obtained in our experiments on two-phase samples of SC-Ol plus Fp are approximately 25% higher than values predicted by the flow law for an equivalent grain size determined in low strain, triaxial compressive creep experiments on single-phase samples of SC-Ol [27]; that is, our two-phase samples are somewhat stronger than their single-phase counterparts. As another comparison, peak stresses in our two-phase samples agree well with those obtained on single-phase aggregates of SC-Ol created from the same starting powders and deformed under similar conditions in torsion in our gas-medium apparatus (figure 6*b*). Similar mechanical behaviour was also observed in two-phase samples of iron-rich Ol and Opx from high-strain torsion experiments performed by Tasaka *et al*. [32]. They noted that their samples were stronger than their single-phase counterparts (their fig. 6).

Furthermore, single-phase aggregates of SC-Ol deformed in torsion at $T = 1473$ K and $P = 300$ MPa by Bystricky *et al*. [30] as well as that deformed in this study (figure 6*a*) exhibited similar initial weakening of 30–40 MPa after reaching the peak stress, obtaining an approximately constant flow stress at $\gamma \geq 4$. The mechanical weakening starting at $\gamma \approx 10$ (figure 4) in our two-phase sample PT-1250 was not observed in single-phase samples of Ol deformed in torsion (CD Meyers & L Hashim, 2018, personal communications). In our two-phase samples (figure 7) and those of Tasaka *et al*. ([32]; their fig. 2), strain localization occurred at $\gamma \gtrsim 10$. This localization in our sample is likely correlated with the decrease in shear stress with increasing shear strain that becomes evident in figure 4 at $\gamma \approx 10$.

(c) Effects of a secondary phase on sample strength

Experiments performed on polycrystalline aggregates of $(Mg_{0.8}Fe_{0.2})O$, both in triaxial compression and in torsion, yielded a value of $n = 4.0 \pm 0.2$ in the dislocation creep regime [22,33]. Based on the flow law developed by Stretton *et al*. [22] and experiments performed on other compositions of ferropericlase [34], $(Mg_{0.9}Fe_{0.1})O$ is expected to be three to four times weaker than SC-Ol when deformed under similar conditions [27]. Results from deformation experiments performed on two-phase aggregates of 80% $(Mg_{0.7}Fe_{0.3})O$ plus 20% SC-Ol demonstrated that the mechanical properties matched those of the weaker phase, in this case, ferropericlase [35].

However, the rheological behaviour of our samples at low strains, near the peak stress is very similar to that observed for single-phase aggregates of SC-Ol deformed in torsion, where both two-phase and single-phase samples have a similar Ol grain size (figure 6*b*) (CD Meyers & L Hashim 2018, personal communications). After this point, at shear strains of $\gamma \gtrsim 4$, our samples containing 30% Fp are stronger than single-phase SC-Ol, having evolved to an Ol grain size almost three times smaller than their single-phase counterparts and maintaining a flow stress larger than or on the order of single-phase samples (figure 6*a*). These observations, along with the similarity of the stress exponent to that determined for single-phase SC-Ol, suggest that the effect of Fp as a weak secondary phase in our two-phase samples is minor. Instead, with increasing strain, more interphase boundaries are created as the frequency of larger Fp grains and clusters of Fp decreases, and more, small Fp grains appear in the Ol matrix. The primary effect of the second phase in this regard is to pin grain boundaries, such that with increasing strain, the Ol grains evolve to a smaller size than that of similarly deformed single-phase samples, leading to weakening and localization at high strains. This behaviour is evidenced by the increased frequency of small particles of Fp in the centre of the sample deformed to $\gamma \approx 14$, where strain localization occurred (figure 7*c*), compared to outside of the area of strain localization, where a number of large clusters of Fp still exist (figure 7*d*). As mentioned above, similar observations were made with two-phase samples of iron-rich Ol plus Opx [32]. These two-phase samples appeared slightly stronger than or similar in strength to single-phase Ol counterparts near the peak stress. The same two-phase samples were then stronger than single-phase Ol at strains of $\gamma \gtrsim 3$ due to smaller grain sizes in the two-phase samples. At high strains, weakening associated with strain localization also occurred in their two-phase samples.

While Tasaka *et al*. [32] attributed the difference in strength between single-phase samples of Fo_{50} and their two-phase samples to the inclusion of Opx, a somewhat stronger phase than Ol, the behaviour of our samples containing 30% Fp, a weaker phase than Ol, suggests a different mechanism is required to explain the observed strengthening.

One possible explanation is that samples buffered at low-silica activity, by the use of Fp, are intrinsically stronger than those buffered at high silica activity, by Opx. Indeed, experiments by Bai *et al*. [36] demonstrated that single crystals of SC-Ol buffered by Fp are stronger than those buffered by Opx at 1523 K and an oxygen fugacity corresponding to an Ni-NiO buffer. This difference could explain the similarity in the strength of our SC-Ol and SC-Ol + Fp samples at the peak stress; specifically, the weakening of Ol due to the presence of a weaker phase (Fp) might be offset by strengthening due to the low-silica activity buffering effect of Fp. However, for fine-grained aggregates of forsterite, Farver & Yund [19] showed that there was no major difference in Si grain boundary diffusion rates when buffered by either excess SiO_2 or excess MgO. This case is more likely to apply to our two-phase samples given their fine grain sizes as well. Additionally, a similar observation in strength difference was reported for the Ol + Opx system [32]. This observation leads us to believe that the change in buffering material does not have a significant effect on the strength of our samples and could not account for the significant strength contrast at large strains given the grain size contrast between the single-phase sample and the two-phase samples (figure 6*a*).

Another possible explanation for the observation that our two-phase samples are stronger than their single-phase counterparts at high strains is associated with the micromechanical processes associated with disGBS. For example, grain boundary sliding and grain boundary migration may be hindered at interphase boundaries compared to grain boundaries. Dislocation glide and climb along interphase boundaries is likely more difficult than along grain boundaries. It has been suggested that glide of dislocations along boundaries, which leads to sliding, is energetically unfavourable due to the disordered structure left behind as a dislocation glides along an interphase boundary [37]. Additionally, grain boundary migration is inhibited due to the inclusion of a secondary phase and, in particular, the presence of interphase boundaries. As established in the Introduction, interphase boundaries pin the surrounding grains from growing by exerting a drag force on boundaries as they migrate [11,12]. These effects would serve to increase the stress required to allow deformation via disGBS processes.

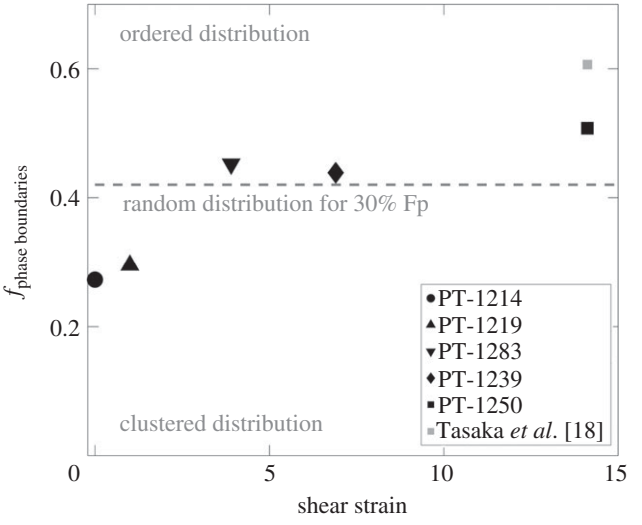

Figure 8. Evolution of interphase boundary fraction with increasing shear strain. The grey dashed line indicates the expected interphase boundary fraction for a random spatial distribution of the minor phase in a sample composed of 30% of a secondary phase [38]. Interphase boundary fractions above and below this line represent ordered and clustered distributions of secondary phases in the material, respectively. The grey square was calculated for comparison from a fit of interphase boundary fraction versus shear strain for samples of 25–33% orthopyroxene and olivine deformed to shear strains of $\gamma > 10$ as determined by Tasaka *et al*. [18].

(d) Microstructural evolution

As shown in figure 8, the fraction of phase boundaries increases from a clustered distribution in the undeformed sample and the sample deformed to low strain ($\gamma = 1.0$) to an ordered distribution in samples deformed to higher strains ($\gamma > 3.0$) [38]. This behaviour is consistent with observations in the low magnification images in figure 2, in which clusters of Fp grains are elongated and form increasingly thin layers with increasing strain, until small grains of Fp are isolated and well distributed among Ol grains at $\gamma = 14.1$. In comparison to the iron-rich olivine (Fo_{50}) plus pyroxene (En_{55}) system of Tasaka *et al*. [18] at shear strains of $\gamma > 10.0$, samples of SC-Ol plus Fp tend toward a more random distribution of the secondary phase.

Compared to the starting and low strain materials, in samples deformed to $\gamma \geq 3.9$ a larger population of small Fp grains appear inside the Ol matrix, farther from clusters of Fp (figure 2*c*,*d*). As this dispersion increases with increasing strain, the grain size distributions in figure 3 become narrower, in that the frequency of clusters of Fp and large grains of Fp and Ol decreases with increasing strain, although the mean grain size does not change significantly. At high strains, small, triangular grains of Fp occur at Ol three- and four-grain junctions, while small elongate grains occur along Ol grain boundaries (figure 2*d*,*e*). Larger grains of Fp often take on distorted shapes as they are impinged upon by rounded Ol grains (figure 11).

(e) Grain size evolution

Microstructural analyses of Åheim and Anita Bay dunite rock deformed in triaxial compression and of SC-Ol single crystals deformed to large strain in direct shear were used to determine a recrystallized grain size piezometer for olivine [39–41]. These studies yielded the relationship

$$d(\mu\text{m}) = 1.5 \times 10^{-8} \times \sigma(\text{MPa})^{-1.33}. \tag{4.1}$$

Their experimental results along with this piezometetric relationship are plotted in figure 9. Grain sizes determined in the present study for aggregates of SC-Ol plus Fp deformed to high strains lie

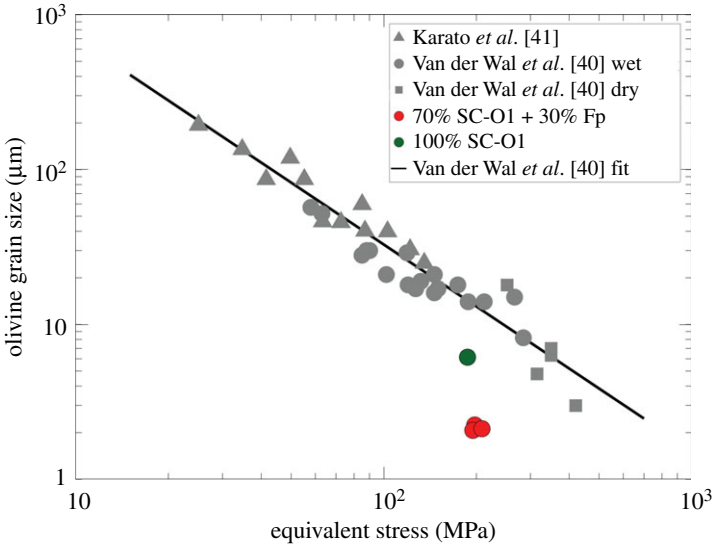

Figure 9. Olivine recrystallized grain size piezometer plotted as grain size versus stress. Grey data points are from studies on olivine single crystals deformed to large shear strain in direct shear [41] and dry and wet natural dunites deformed in triaxial compression [40]. The black line is the piezometric relationship determined by a fit through the data [40]. Red circles are the stress–grain size data determined in this study on two-phase aggregates of 70% SC-Ol + 30% Fp deformed to shear strains of $\gamma > 3$. The green circle represents the stress–grain size data for the single-phase aggregate of SC-Ol deformed to $\gamma > 3$.

approximately a factor of 10 below the piezometer, while single-phase SC-Ol lies approximately within a factor of 2 of the piezometer, much closer to this relationship. Similar behaviour has been reported for other polymineralic systems [7,32]. This observation indicates that grain size is not simply controlled by the competition between dynamic recrystallization and grain growth.

For two-phase systems, the grain size in a steady-state is expected to follow the Zener relation

$$\frac{d_{\mathrm{I}}}{d_{\mathrm{II}}} = \frac{c}{{f_{\mathrm{II}}}^{m}}, \tag{4.2}$$

where d_{I} is the grain size of the primary phase, in this case Ol, d_{II} is the grain size of the secondary phase, f_{II} is the fraction of secondary phase present in the rock, c is a constant, and m is an exponent that has been related to the distribution geometry of secondary phase particles [10,11]. Values for the parameters in equation (4.2) for the olivine-orthopyroxene system have been determined from laboratory experiments [42,43]. A comparison of the ratios between grain sizes of both phases in this study to those found in experiments on aggregates of Fo_{50} plus En_{55} for a fraction of secondary phase particles ($f_{\mathrm{II}} = 26\%$) similar to that used in our experiments is displayed in figure 10. The fit parameters $c = 0.74$ and $m = 0.59$ used by Tasaka *et al.* [18] yield good agreement with grain size ratios of our samples of SC-Ol plus Fp at high strains. At these fractions of secondary phase particles, this result suggests that the olivine-ferropericlase system has similar Zener parameters, as well as a similar geometrical distribution of the second phase to the olivine-orthopyroxene system [18] and other natural polymineralic samples [8]. A value of $m \approx 0.5$ indicates that second-phase particles are predominately at grain boundaries of the primary phase, instead of at three- and four-grain junctions for which $m \approx 0.3$ [10,11]; this conclusion is supported by images of highly strained samples, for example, as in figure 11. Note that the fit in figure 10 does not go through the grain size values determined for the starting and clustered material from this study. Grain sizes determined in our experiments only trend toward the fit once the system is dominated by an ordered distribution rather than a clustered distribution.

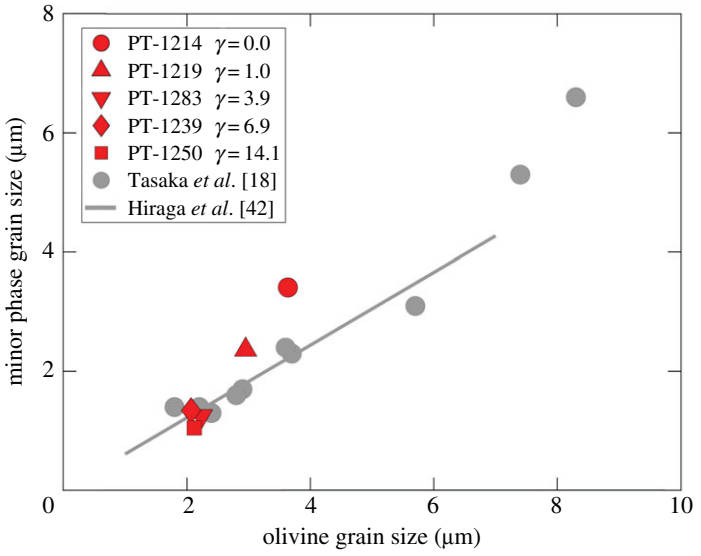

Figure 10. Ferropericlase grain size versus olivine grain size from our undeformed and deformed samples plotted with orthopyroxene versus olivine grain size data from Tasaka *et al*. [18] (grey circles) and the Zener relation determined by Hiraga *et al*. [42] for the orthopyroxene-olivine system (grey line).

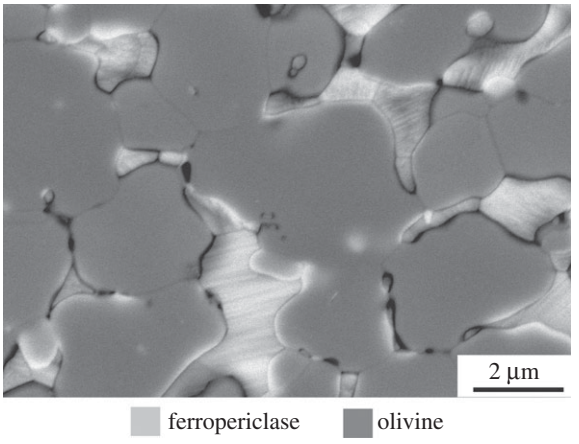

Figure 11. High-magnification BSE micrograph of sample PT-1250. The lighter phase is ferropericlase, and the darker grey phase is San Carlos olivine.

(f) Mechanisms of phase mixing

As detailed in the Introduction, recent studies have invoked both mechanical and chemical processes to explain the observations associated with phase mixing in two-phase samples. Similarities to each of these models are observed in the microstructures from samples deformed in our study. Figure 2*c* displays an example of a single layer of Ol grains isolated between clusters of Fp; in addition, individual grains of Ol are in the process of being isolated from one another, as proposed by the model for mechanical mixing detailed by Cross & Skemer [16]. The small grains of Fp throughout the Ol matrix in figures 2*c–e* are reminiscent of particles seen in experiments performed by Tasaka *et al*. [18]. Long, small grains of Fp along Ol grain boundaries and cuspate

features on larger grains of Fp in both figures 2*c–e* and figure 11 resemble the 'teeth' discussed by Bercovici & Skemer [17].

Cross & Skemer [16] define the evolution to a mixed state in their two-phase system by an increase in phase boundary fraction associated with the thinning and elongation of individual layers of both phases with increasing strain. Similar behaviour was observed by Tasaka *et al*. [18] and in our study, as demonstrated in figure 8. However, at the scale of the grain size, observations in our study are more similar to the models proposed by Tasaka *et al*. [18] and Bercovici & Skemer [17]. The frequency of small Fp grains found in the Ol matrix, distant (tens of micrometres) from any sources of larger Fp grains, is not explained solely by the thinning of layers and requires another mechanism for this sort of mixing. Moving grains this far into the matrix can be accomplished by stress gradients between grain boundaries due to the applied stress during deformation or chemical diffusion of MeO units in response to the established stress gradients mentioned previously [17,18]. Such processes transport small particles of the secondary phase into the Ol matrix where they act to pin grain boundaries.

In the centre of the high-magnification image of figure 2*c*, a progression of Ol grains was captured as they were being separated from their parent layer. This evolution in microstructure appears to be accomplished by the formation of cuspate features on layers of Fp that interconnect when layers are near enough spatially or by the build-up of small Fp grains along Ol grain boundaries that also connect nearby layers of Fp. Both of these processes serve to isolate individual grains of Ol, thereby pinning their grain boundaries. Although these cuspate features bear a striking resemblance to the teeth predicted by the mechanical mixing model of Bercovici & Skemer [17], because the model of Tasaka *et al*. [18] relies on the diffusion of MeO into grain boundaries of olivine in deviatoric tension, it is still possible that the small particles of Fp we observe along these boundaries and at three- and four-grain junctions in the matrix were transported by diffusional mass transport of MeO. Owing to the similarities between the predictions of these mixing models, it is as of yet unclear which mechanism dominates in our experiments.

Finally, we return to consider the localized deformation that occurred in our sample deformed to the highest strain of $\gamma > 14$, PI-1250. This two-phase aggregate underwent strain localization as deformation concentrated into a shear band cutting horizontally through the approximate centre of the thin-walled cylindrical sample. As previously mentioned, this localization is likely associated with the abrupt strain weakening observed in figure 4 at a strain of $\gamma \approx 10$. Similar strain localization was observed in the Ol + Opx samples deformed to high strains by Tasaka *et al*. [32]. Such localization of strain into a narrow shear zone is associated with a significant enhancement in two-phase mixing (figure 7*c*,*d*), and additional reduction in grain size thus forming a positive feedback loop, whereby deformation is localized into regions with a smaller average grain size, leading to further grain size reduction and weakening, and maintaining localization in these regions over long periods of time. Similar behaviour is expected to occur in nature, enabling a shear zone to form in regions of well-mixed, multi-phase grains of a deforming rock mass.

Data accessibility. This article has no additional data.

Authors' contributions. H.S.W. carried out the experiments, performed the data analysis, and drafted the manuscript. M.E.Z. and D.L.K. conceived of and helped to design the study and provided revisions of the manuscript. All authors read and approved the manuscript.

Competing interests. We declare we have no competing interests.

Funding. This study was funded by NASA grant NNX15AL53G (D.L.K.), NSF grant EAR-1755498 (M.E.Z.). Part of this work was carried out in the Characterization Facility at the University of Minnesota - Twin Cities, which receives partial support from NSF through the MRSEC program.

Acknowledgements. The authors thank A. Dillman L. Hashim C. Meyers and C. Qi for valuable discussion about and assistance with experiments. We would also like to thank the reviewers for their insightful comments and detailed reviews. We thank the Characterization Facility at the University of Minnesota - Twin Cities for the use of their SEM.

References

1. Tackley P. 2000 The quest for self-consistent generation of plate tectonics in mantle convection models. In *The history and dynamics of global plate motions* (eds MA Richards, RG Gordon, RD van der Hilst), vol. 121, pp. 47–72. Geophysical monograph series. Washington, DC: American Geophysical Union.
2. Bercovici D, Tackley P, Ricard Y. 2015 The generatio of plate tectonics from mantle dynamics. In *Treatise on geophysics* (eds D Bercovici, G Schubert), Mantle dynamics, vol. 7, pp. 271–318. New York, NY: Elsevier.
3. Bercovici D, Ricard Y. 2016 Grain-damage hysteresis and plate tectonic states. *Phys. Earth Planet. Inter.* **253**, 31–47. (doi:10.1016/j.pepi.2016.01.005)
4. Skemer P, Warren JM, Hansen LN, Hirth G, Kelemen PB. 2013 The influence of water and LPO on the initiation and evolution of mantle shear zones. *Earth Planet. Sci. Lett.* **375**, 222–233. (doi:10.1016/j.epsl.2013.05.034)
5. Warren JM, Hirth G. 2006 Grain size sensitive deformation mechanisms in naturally deformed peridotites. *Earth Planet. Sci. Lett.* **248**, 438–450. (doi:10.1016/j.epsl.2006.06.006)
6. Hansen LN, Warren JM. 2015 Quantifying the effect of pyroxene on deformation of peridotite in a natural shear zone. *J. Geophys. Res. Solid Earth* **120**, 2717–2738. (doi:10.1002/2014JB011584)
7. Linckens J, Herwegh M, Muntener O, Mercolli I. 2011 Evolution of a polymineralic mantle shear zone and the role of second phases on the localization of deformation. *J. Geophys. Res.* **116**, B06210. (doi:10.1029/2010JB008119)
8. Ambrose TK, Wallis D, Hansen LN, Waters DJ, Searle MP. 2018 Controls on the rheological properties of peridotite at a palaeosubduction interface: a transect across the base of the Oman–UAE ophiolite. *Earth Planet. Sci. Lett.* **491**, 193–206. (doi:10.1016/j.epsl.2018.03.027)
9. Bercovici D, Ricard Y. 2012 Mechanisms for the generation of plate tectonics by two-phase grain-damage and pinning. *Phys. Earth Planet. Inter.* **202–203**, 27–55. (doi:10.1016/j.pepi.2012.05.003)
10. Evans B, Renner J, Hirth G. 2001 A few remarks on the kinetics of static grain growth in rocks. *Int. J. Earth Sci.* **90**, 88–103. (doi:10.1007/s005310000150)
11. Manohar PA, Ferry M, Chandra T. 1998 Five decades of the Zener equation. *ISIJ Int.* **38**, 913–924. (doi:10.2355/isijinternational.38.913)
12. Smith CS. 1948 Grains, phases, interfaces: an interpretation of microstructures. *Trans. Amer. Inst. Min. Metall. Eng.* **175**, 15–51.
13. Czertowicz TA, Toy VG, Scott JM. 2016 Recrystallisation, phase mixing and strain localisation in peridotite during rapid extrusion of sub-arc mantle lithosphere. *J. Struct. Geol.* **88**, 1–19. (doi:10.1016/j.jsg.2016.04.011)
14. Newman J, Lamb WM, Drury MR, Vissers RLM. 1999 Deformation processes in a peridotite shear zone: reaction-softening by an H_2O-deficient continuous net transfer reaction. *Tectonophysics* **303**, 193–222. (doi:10.1016/S0040-1951(98)00259-5)
15. Precigout J, Stunitz H. 2016 Evidence of phase nucleation during olivine diffusion creep: a new perspective for mantle strain localization. *Earth Planet. Sci. Lett.* **455**, 94–105. (doi:10.1016/j.epsl.2016.09.029)
16. Cross AJ, Skemer P. 2017 Ultramylonite generation via phase mixing in high-strain experiments. *J. Geophys. Res. Solid Earth* **122**, 1744–1759. (doi:10.1002/2016JB013801)
17. Bercovici D, Skemer P. 2017 Grain damage, phase mixing and plate-boundary formation. *J. Geodyn.* **108**, 40–55. (doi:10.1016/j.jog.2017.05.002)
18. Tasaka M, Zimmerman ME, Kohlstedt DL, Stünitz H, Heilbronner R. 2017 Rheological weakening of olivine + orthopyroxene aggregates due to phase mixing: Part 2. Microstructural development. *J. Geophys. Res. Solid Earth* **122**, 7597–7612. (doi:10.1002/2017JB014311)
19. Farver JR, Yund RA. 2000 Sillicon diffusion in forsterite aggregates: Implications for diffusion accommodated creep. *Geophys. Res. Lett.* **27**, 2337–2340. (doi:10.1029/2000GL008492)
20. Dohmen R, Chakraborty S, Becker HW. 2002 Si and O diffusion in olivine and implications for characterizing plastic flow in the mantle. *Geophys. Res. Lett.* **29**, 2030. (doi:10.1029/2002GL015480)
21. Gardés E, Wunder B, Wirth R, W H. 2011 Growth of multilayered polycrystalline reaction rims in the MgO-SiO_2 system, part I: Experiments. *Contrib. Mineral. Petrol.* **161**, 1–12. (doi:10.1007/s00410-010-0517-z)

22. Stretton I, Heidelbach F, Mackwell S, Langenhorst F. 2001 Dislocation creep of magneseowüstite ($Mg_{0.8}Fe_{0.2}O$). *Earth Planet. Sci. Lett.* **196**, 229–240. (doi:10.1016/S0012-821X(01)00533-7)
23. Paterson MS. 1990 Rock Deformation Experimentation. In *The brittle ductile transition in rocks, The heard volume* (eds AG Duba, WB Durham), geophysical monograph series, vol. 56, pp. 187–194. Washington, DC: American Geophysical Union.
24. Hansen LN, Zimmerman ME, Kohlstedt DL. 2012 The influence of microstructure on deformation of olivine in the grain-boundary sliding regime. *J. Geophys. Res. Solid Earth* **117**, B09201. (doi:10.1029/2012JB009305)
25. Paterson M, Olgaard D. 2000 Rock deformation tests to large shear strains in torsion. *J. Struct. Geol.* **22**, 1341–1358. (doi:10.1016/S0191-8141(00)00042-0)
26. Frost H, Ashby M. 1982 *Deformation mechanism maps*. New York, NY: Pergamon.
27. Hansen LN, Zimmerman ME, Kohlstedt DL. 2011 Grain boundary sliding in San Carlos olivine: Flow law parameters and crystallographic-preferred orientation. *J. Geophys. Res.* **116**, B08201. (doi:10.1029/2011JB008220)
28. Wang Z, Zhao Y, Kohlstedt DL. 2010 Dislocation creep accommodated by grain boundary sliding in dunite. *J. Earth Sci.* **21**, 541–554. (doi:10.1007/s12583-010-0113-1)
29. Langdon TG. 2006 Grain boundary sliding revisited: developments in sliding over four decades. *J. Mater. Sci.* **41**, 597–609. (doi:10.1007/s10853-006-6476-0)
30. Bystricky M, Kunze K, Burtini L, Burg JP. 2000 High shear strain of olivine aggregates: Rheological and seismic consequences. *Science* **290**, 1564–1567. (doi:10.1126/science.290.5496.1564)
31. Keefner JW, Mackwell SJ, Kohlstedt DL, Heidelbach F. 2011 Dependence of dislocation creep of dunite on oxygen fugacity: implications for viscosity variations in Earth's mantle. *J. Geophys. Res.* **116**, B05201. (doi:10.1029/2010JB007748)
32. Tasaka M, Zimmerman ME, Kohlstedt DL. 2017 Rheological weakening of olivine + orthopyroxene aggregates due to phase mixing: 1. Mechanical behavior. *J. Geophys. Res. Solid Earth* **122**, 7584–7596. (doi:10.1002/2017JB014333)
33. Heidelbach F, Stretton I, Langenhorst F, Mackwell S. 2003 Fabric evolution during high strain shear deformation of magnesiowüstite ($Mg_{0.8}Fe_{0.2}O$). *J. Geophys. Res.* **108**, 2154. (doi:10.1029/2001JB001632)
34. Heidelbach F, Terry MP, Bystricky M, Holzapfel C, McCammon C. 2008 A simultaneous deformation and diffusion experiment: quantifying the role of deformation in enhancing metamorphic reactions. *Earth Planet. Sci. Lett.* **278**, 386–394. (doi:10.1016/j.epsl.2008.12.026)
35. Bystricky M, Heidelbach F, Mackwell S. 2006 Large-strain deformation and strain partitioning in polyphase rocks: dislocation creep of olivine-magnesiowüstite aggregates. *Tectonophysics* **427**, 115–132. (doi:10.1016/j.tecto.2006.05.025)
36. Bai Q, Mackwell SJ, Kohlstedt DL. 1991 High-temperature creep of olivine single crystals 1: mechanical results for buffered samples. *J. Geophys. Res.* **96**, 2441–2463. (doi:10.1029/90JB01723)
37. Gittus JH. 1977 Theory of superplastic flow in two-phase materials: roles of interphase-boundary dislocations, ledges, and diffusion. *J. Eng. Mater. Technol.*, 244–251. (doi:10.1115/1.3443527)
38. Heilbronner R, Barrett S. 2014 *Image analysis in earth science: microstructures and textures of earth materials*, 1st edn, pp. 351–368. Berlin, Germany: Springer.
39. Twiss RJ. 1977 Theory and applicability of a recrystallized grain size paleopiezometer. *Pure Appl. Geophys.* **115**, 227–244. (doi:10.1007/BF01637105)
40. Van der Wal D, Chopra P, Drury M, FitzGerald JD. 1993 Relationships between dynamically recrystallized grain size and deformation conditions in experimentally deformed olivine rocks. *Geophys. Res. Lett.* **20**, 1479–1482. (doi:10.1029/93GL01382)
41. Karato S-I, Toriumi M, Fujiji T. 1980 Dynamic recrystallization of olivine single crystals during high-temperature creep. *J. Geophys. Res.* **7**, 649–652. (doi:10.1029/GL007i009p00649)
42. Hiraga T, Tachibana C, Ohashi N, Sano S. 2010 Grain growth systematics for forsterite ± enstatite aggregates: effect of lithology on grain size in the upper mantle. *Earth Planet. Sci. Lett.* **291**, 10–20. (doi:10.1016/j.epsl.2009.12.026)
43. Tasaka M, Hiraga T. 2013 Influence of mineral fraction on the rheological properties of forsterite + enstatite during grain size sensitive creep: 1. Grain size and grain growth laws. *J. Geophys. Res. Solid Earth* **118**, 1–21. (doi:10.1002/jgrb.50285)